Applied Catalysis B: Environmental 286 (2021) 119942

Contents lists available at ScienceDirect

Applied Catalysis B: Environmental

journal homepage: www.elsevier.com/locate/apcatb

Highly selective Ru/HBEA catalyst for the direct amination of fatty alcohols with ammonia

L. Fang [a,*,1], Z. Yan [a], J. Wu [b], A. Bugaev [c], C. Lamberti [c,d,2], M. Pera-Titus [a,*]

[a] Eco-Efficient Products and Processes Laboratory (E2P2L), UMI 3464 CNRS – Solvay, 3966 Jin Du Road, Xin Zhuang Ind. Zone, 201108, Shanghai, China
[b] Solvay (China) Co., Ltd, 3966 Jin Du Road, Xin Zhuang Ind. Zone, 201108, Shanghai, China
[c] The Smart Materials Research Institute, Southern Federal University, Sladkova 178/24, 344090, Rostov-on-Don, Russia
[d] Department of Chemistry, CrisDi Centre for Crystallography, University of Torino, via Giuria 7, 10125, Torino, Italy

ARTICLE INFO

Keywords:
1-octanol
Ammonia
H_2borrowing
Ruthenium
Zeolite

ABSTRACT

The present study describes the synthesis of primary amines from long-chain fatty alcohols and ammonia using supported ruthenium catalysts over different acid supports, including a variety of zeolites with different topologies and Si/Al ratios. The morphology, acidity and location of ruthenium in the catalysts was studied in detail by combining XRD, BET, HR-TEM, NH_3-TPD, octylamine-TPD, H_2-TPR, XPS, EXAFS / XANES, ^{27}Al MAS NMR and TGA. In particular, Ru/HBEA (Si/Al = 25) with 5 wt% Ru afforded more than 90 % conversion and 90 % selectivity to 1-octylamine in the liquid-phase amination reaction of 1-octanol with ammonia at 180 °C in a batch reactor. The high selectivity of Ru/HBEA (Si/Al = 25) can be explained by the presence of Brønsted / Lewis acid centers with medium strength in the proximity of ruthenium nanoparticles. The catalyst was further tested in a pre-pilot continuous stirred-tank reactor (2 L) with flash separation of 1-octylamine. In this configuration, a steady 92 % selectivity of octylamine was obtained at 87 % 1-octanol conversion during 120 h on steam. The catalyst kept its integrity during the reaction.

1. Introduction

Alkylamines derived from fatty acids, olefins or alcohols are relevant intermediates in the bulk and fine chemical industries for the production of polymers, dyes, pharmaceuticals, agrochemicals, surfactants and biologically active compounds [1,2]. The available technologies for alkylamine synthesis usually encompass the use of hazardous reagents (*e.g.*, HCN) or generate hazardous by-products (*e.g.*, HCl), making the preparation of amines hardly sustainable. As an alternative, the direct amination of alcohols with ammonia emerges as an atom-efficient and environmentally benign process, since water is generated as sole by-product without waste salts [2–4]. This process is also compatible with biorefineries, which are expected to supply a large portfolio of alcohols [5]. Among the possible amines, primary amines issued from the alkylation of ammonia with fatty alcohols are useful intermediates for further derivatization reactions. However, selectivity to primary amines at high alcohol conversion is thermodynamically discouraged in detriment of secondary amines [6,7].

The most studied catalysts for the direct synthesis of primary alkylamines rely on Raney Ni [8,9], as well as Ni [10–12] and Co [13,14] supported over alkaline or amphoteric oxides (*e.g.*, γ,θ-Al_2O_3). However, at higher temperatures and low NH_3 excess with respect to the alcohol (>3 equiv), these formulations favor the formation of mixtures of primary, secondary and tertiary amines for short-chain alcohols (<C_4) with yields well below 50 % [13,15–18]. Besides, as a rule, these formulations encompass large metal contents (most often >15 wt%) and are prone to metal leaching upon exposure to ammonia and polar solvents, thereby favoring the contamination of the amine product by the metal. This shortcoming can limit the application of the amines as additives in personal care products.

Ruthenium nanoparticles, either unsupported or supported over metal oxides and carbon, can afford high selectivity to primary amines in the reductive amination of aromatic, furanic and aliphatic aldehydes/ketones with NH_3 and H_2 [19–22], and in the direct amination of alcohols [23–25]. Support effects were evidenced on the performance of supported Ru, which has special impact on the reductive amination of

* Corresponding authors.
E-mail addresses: lin.fang@basf.com (L. Fang), marc.pera-titus-ext@solvay.com (M. Pera-Titus).
[1] Current address: BASF Catalysts (Shanghai) Co. Ltd., 239 Luqiao Export Process Zone, Pudong, 201206 Shanghai, China.
[2] Deceased.

https://doi.org/10.1016/j.apcatb.2021.119942
Received 23 November 2020; Received in revised form 21 January 2021; Accepted 24 January 2021
Available online 29 January 2021

furfural to furfurylamine. In particular, Ru/Nb_2O_5 was very efficient for this reaction compared to Ru/TiO_2 and $RuSiO_2$, which was attributed to a lower electron density of Ru particles in the presence of Nb_2O_5 [21]. The presence of acid centers, either Brønsted or Lewis, near Ru nanoparticles can favor the stabilization of intermediate primary and secondary imines in the reductive amination of aldehydes and ketones, facilitating their hydrogenation [21,22,26]. Besides, surface acidity, which can be induced by the presence of unreduced RuO_2 [21,27,28], is known to promote the hydrogenation of C═N, C═O and C═C bonds by metal ruthenium [19,29–33], as well as the hydrogenolysis of OH groups in biobased reagents [34–37].

Herein we show that the selectivity of ruthenium nanoparticles towards primary alkylamines can be strongly enhanced at high alcohol conversion by the presence of Brønsted acid centers in the proximity of ruthenium nanoparticles. To this aim, we prepared a series of ruthenium catalysts by aqueous impregnation over different acid supports, including a variety of zeolites with different topologies and Si/Al ratios, and γ-alumina. The morphology, acidity and location of ruthenium in the catalysts was studied in detail by combining X-ray diffraction (XRD), BET, high-resolution transmission electron microscopy (HR-TEM), temperature-programmed NH_3 desorption (NH_3-TPD), temperature-programmed reduction (H_2-TPR), x-ray photoelectron spectroscopy (XPS), X-ray absorption spectroscopy (EXAFS), solid-state ^{27}Al magic angle nuclear magnetic resonance (^{27}Al MAS NMR), and thermogravimetric analysis (TGA), while the catalytic performance was assessed in the liquid-phase amination reaction of 1-octanol (OL) and ammonia NH_3 both in batch and pre-pilot continuous stirred-tank reactors, as a model amination reaction of fatty alcohols issued from vegetable oils.

2. Experimental

2.1. Materials

HBEA(25) (Si/Al = 25), HBEA(150) (Si/Al = 150), HBEA(300) (Si/Al = 300) and HZSM-5(20) (Si/Al = 20) (Clariant, 550-650 m^2/g), 5% Ru/C (Johnson Matthey, 782 m^2/g), HY (Si/Al = 10) (Zeolyst, 850 m^2/g), SiO_2 (Sasol, 187 m^2/g), MgO (Sinopharm, 39 m^2/g), γ-Al_2O_3 (Puralox Sasol Scca-5/170, 154 m^2/g) were used as supports for catalysts synthesis. Ruthenium chloride hydrate ($RuCl_3 \cdot xH_2O$, Ru content 45–55 %, purity >99.5 wt.%), supplied by Sigma-Aldrich), was used as precursor for Ru impregnation. 1-Octanol (>99.8 wt.%), t-amyl alcohol and sodium chloride (>99.8 wt.%) were procured from Sinopharm, while 1-hexanol was supplied by Sigma-Aldrich (>99.8 wt.%)). NH_3 and N_2 were supplied by Air Liquide (purity 99.99 %). H_2 was obtained from a H_2 generator from ANPEL (LGH-500 T). Hydrazine hydrate (50–60 %, Merck) was used as reducing reagent. Octylamine (OA), dioctylamine (DOA), trioctylamine (TOA) and octanenitrile (ON) standards for GC calibration were all purchased from J&K (purity 99.5 %). Biphenyl (99.5 % purity), supplied by J&K Scientific, was used as standard for GC calibration. All the reactants were used as received without further purification.

2.2. Catalyst preparation

Ruthenium was loaded (5−10 wt.%) over the Al_2O_3, SiO_2, MgO, HBEA, HY and HZSM-5 by wet impregnation method using an aqueous solution of the ruthenium precursor. In a typical preparation (5 wt.% Ru), 0.3079 g of $RuCl_3 \cdot xH_2O$ was dissolved in 3.6 mL of deionized water in the presence of 3.0 g of the given support, and the suspension was vigorously stirred at room temperature for 2 h. After this period, the solid was dried at 60 °C under vacuum and calcined at 450 °C for 6 h under static air, generating a ruthenium oxide phase on the support. The solid was then reduced for 1 h at variable temperatures according to the H_2-TPR profiles in a quartz tube under a 25v/v% H_2/N_2 flow [35 cm^3(STP)/min] using a heating rate of 5 °C.min^{-1}, resulting in the final metallic Ru-loaded catalyst. Using this protocol, different catalysts were prepared, which are hereinafter termed as Ru/HBEA(25), Ru/HBEA(150), Ru/HBEA(300), Ru/HZSM-5(20), HY(10), Ru/Al_2O_3, Ru/SiO_2 and Ru/MgO. Finally, a Ru/HBEA(25) catalyst was prepared at large volume (5 kg) with the above protocol, but using hydrazine hydrate instead of H_2 a reducing agent. The use of hydrazine instead of H_2 did not exert any impact on the catalyst morphology and catalytic activity.

For comparison, a Ru catalyst over Na-exchanged HBEA was also prepared. Briefly, the parent HBEA(25) was first subjected to ion-exchange by Na^+ using a saturated NaCl solution. Two samples were prepared, namely 1NaBEA(25) and 2NaBEA(25), referring to one and two ion-exchange steps, respectively. After ion exchange, the samples were dried and activated at 500 °C for 3 h, and were further impregnated with Ru with the same loading using the same protocol as for Ru/HBEA (25). The final catalysts are hereinafter termed as Ru/1NaBEA(25) and Ru/2NaBEA(25).

2.3. Catalyst characterization

The Ru content in the catalysts was quantified by wavelength dispersive X-ray Fluorescence (WDXRF, Malvern Panalytical Zetium) using the Omnian-2.4kW-He method.

Powder XRD (PXRD) was used to characterize the phases present in the catalysts. The PXRD patterns were measured on a Rigaku D8 D/max 2200v/pc diffractometer operated at 40 mA and 40 kV using Cu K_α radiation (λ =1.54178 Å). The patterns were collected in the 2θ range 5−50° at a scan rate of 4°.min^{-1} and a step size of 0.01°. The patterns were indexed using the Joint Committee on Powder Diffraction (JCPDS) database and interpreted using MDI JADE 5.0 software. The Scherrer equation was used to estimate the average crystallite size of RuO_x particles from the width at half-height of the most intense peaks of the diffraction pattern.

The specific surface area and pore volume of the catalysts was measured by N_2 adsorption at −196 °C using a Micromeritics ASAP 2010 Surface Area Analyzer. The surface areas were calculated by the Brunauer-Emmett-Teller (BET) method in the relative pressure range $0.05 < P/P_0 < 0.30$, while the pore volume was measured at $P/P_0 = 0.97$. The average pore size was measured using the Barrer-Joyner-Halenda (BJH) method. Prior to the measurements, the catalysts were degassed at 180 °C for 3 h under vacuum (0.5 mbar).

The size distribution of Ru nanoparticles was measured by HR-TEM using a JEOL, JEM-2100 (200 kV) microscope equipped with a LaB_6 electron gun. The images were analyzed by ImageJ software. At least 200 particles were counted for the statistic chart. In the analyses, we assumed that the metal particles are spherical in shape and we took explicitly into account the density ratio between the oxide and metal phases. The average particle size (surface weighted, $d_p[3,2]$) was estimated from the particle size distribution using the expression [38]

$$d_p[3,2] = \frac{\sum_{i=1}^{i=n} d_{p,i}^3 n_i}{\sum_{i=1}^{i=n} d_{p,i}^2 n_i} \quad (1)$$

The metal dispersion, D, was measured from the average particle size according to the expression [38]

$$D(\%) = 6\frac{M_i}{\rho_i}\frac{1}{N_A \pi r_i^2}\frac{1}{d_p} \quad (2)$$

where ρ_i is the metal density, N_A is the Avogadro Number, r_i is the covalent radius of the metal and d_p is the average size of metal nanoparticles measured by HR-TEM.

The distribution of acid sites on the catalysts was measured by NH_3-TPD. The profiles were acquired on a Micromeritics AutoChem II 2920 instrument provided with a quartz U-type reactor, a thermal conductivity detector (TCD) and a cold trap with frozen isopropanol before the detector. Before the tests, the given catalyst (60 mg) was degassed at 300

°C for 2 h under He flow [40 m L(STP)/min]. The catalyst was then exposed to a flow of 10 % NH_3-He [40 m L(STP)/min] for 20 min. After purging under He for 30 min, the catalyst was heated to 700 °C under He flow at 10 °C.min^{-1}. The OA-TPD profiles were measured in the same instrument at similar conditions. Prior to desorption, the samples were saturated with OA pulses using a built-in vapor generator.

The temperature-programmed reduction (H_2-TPR) profiles were measured on a Micromeritics AutoChem II 2920 instrument. The given catalyst was first pre-reduced in a quartz tube under 10%H_2-Ar flow [40 mL(STP)/min] in the temperature range 30−1000 °C at 10 °C.min^{-1}. Before each test, the catalyst was heated to 300 °C for 2 h under a He flow [40 mL(STP)/min] followed by cooling down to 40 °C.

Pulse CO chemisorption was carried out using a Micromeritics AutoChem II 2920 instrument. Briefly, the given calcined catalyst (100 mg) was reduced under a 10 % H_2-Ar flow [40 mL(STP)/min] at 580 °C for 30 min at 10 °C.min^{-1}. Then, the sample was cooled down to 50 °C and purged with He [20 mL(STP)/min] for 20 min. CO chemisorption was carried out by introducing consecutive 10 % CO-He pulse doses until saturation. The stoichiometry factor S. F. between the metal atoms and CO molecules was assumed to be 2.

The ^{27}Al MAS NMR spectra were measured on a DSX Bruker spectrometer operated using a 3.2 mm MAS probe head at 18.8 T and at a ^{27}Al Larmor frequency of 208.6 MHz. The spectra were recorded at a spinning rate of 20 kHz using a single pulse excitation sequence with small pulse angle ($\phi = 12$) and a recycle delay of 4 s. The chemical shifts were referenced to a 1 M $Al(NO_3)_3$ aqueous solution.

The surface composition of the catalysts was analyzed by XPS using a Thermo ESCALAB 250 spectrometer with monochromatic Al Kα radiation ($h\nu$ =1486.6 eV). The spectra were recorded using an Al monochromated X-ray source (15 kV, 15 mA) with a pass energy of 30 eV (0.05 eV/step) for high resolution spectra, and a pass energy of 70 eV (1 eV/step) for survey spectrum in hybrid mode and slot lens mode, respectively. The adventitious C1s binding energy (284.9 eV) was used as internal reference.

In situ XAS experiments were performed to monitor the oxidation and coordination state of Ru along activation and catalysis [39]. X-ray absorption near-edge structure (XANES) and extended X-ray absorption fine structure (EXAFS) spectra at Ru *K*-edge were measured at the BM26A beamline (now moved to BM14 port) of the European Synchrotron Radiation Facility (ESRF, Grenoble, France). The spectra were collected in transmission mode by ionization chambers in the energy range 21.9–23.4 keV, with the step ΔE =5 eV in the pre-edge region, ΔE =1 eV in the XANES region, and the constant step in the photoelectron momentum space Δk =0.05 Å^{-1} in the EXAFS region. The energy was selected by Si(111) double crystal and silicon mirrors were used for the rejection of higher harmonics. The acquisition time was set to 1 s/point for the pre-edge and XANES regions, and was grown quadratically from 1 to 2 s/point in the EXAFS region. The sample was pressed into a pellet and placed inside the microtomo cell connected to a remotely controlled gas line [40]. The cell had a built-in heater and thermocouple allowing a fine control of the temperature in the range from 30 to 450 °C. The pure He, 20%O_2/He, 10%H_2/He and 5%NH_3/He flowrate was regulated using mass flow controllers. The alcohol vapors (1-hexanol instead of 1-octanol due to the lower boiling point of the former) were introduced into the gas flow using a glass saturator. The output of the cell was analyzed by means of Pfeiffer Omnistar online mass spectrometer. The experimental spectra were processed using Demeter software by Fourier-transformation (FT) [41]. The fitting of FT-EXAFS data was performed in *R*-space with theoretical phases and amplitudes calculated in FEFF6 code [42]. The changes in the XANES region during catalyst activation were quantified by linear combination fittings.

EXAFS spectroscopy gives an indirect quantification of the particle size based on the average coordination number. In particular, assuming a spherical shape of the nanoparticles, the particle size can be calculated based on coordination numbers and interatomic distances using the size equation reported by Calvin et al. [43]. Due to the non-linear dependency, a relatively small error of ± 0.8 (within 10%) in coordination number results in quite broad range for particle sizes.

2.4. Catalytic tests in batch reactor

The catalytic activity of the Ru catalysts was assessed for OL amination with NH_3 (Scheme 1). The reaction was carried out in a 30-mL stainless steel autoclave equipped with a pressure gauge and a safety valve. In a typical test, the reactor was charged with OL (6.3 mmol) and 250 mg of catalyst. The reactor was sealed and purged using N_2 followed by charging NH_3 (8 bar) and H_2. The reactor was then placed on a hot plate equipped with a magnetic stirrer and heated to 180 °C. At these conditions, the nominal NH_3/OL molar ratio was about 4.6−8.0. The stirring rate was kept at a value higher than 600 r.p.m, since the OL conversion and selectivity over Ru/HBEA(25)_4 were found to be unaffected by the stirring rate, pointing out a lack of external mass transfer effects on the reaction rate according to preliminary results.

The reactant (OL) and the expected N-products, i.e. OA, DOA, TOA, ON, were analyzed and quantified after the reaction using an Agilent 7890 GC equipped with a HP-5 capillary column with 5 wt.% phenyl groups and a FID detector. Biphenyl was used as internal standard. The carbon balance (CB) were accurate to within 5–15 % for all the catalytic tests.

The OL conversion (limiting reactant) and the selectivity to the N-containing products were defined as follows:

$$\text{Conversion}\ (\%) = 1 - \frac{n_{OL}}{n_{OL}^0} \tag{3}$$

$$\text{Selectivity}_i\ (\%) = \frac{n_i}{\sum_i n_i} \quad i = 1 \ldots N - \text{products} \tag{4}$$

$$CB = \frac{\sum_i n_i + n_{OL}}{n_{OL}^0} \tag{5}$$

where n_{OL}^0 and n_{OL} refer to the initial and final mole number of OL, respectively, whereas n_i corresponds to the mole number of N-containing products formed.

The turnover frequency (TOF) was measured by dividing the number of moles of OA formed at 10 % OL conversion by the number of moles of surface Ru and the time

$$TOF\left(h^{-1}\right) = \left.\frac{n_{OA}}{n_{Ru}^S t}\right|_{Conv=10\%} \tag{6}$$

2.5. Catalytic tests in continuous stirred tank reactor (CSTR)

A catalytic test was carried out in CSTR (2 L) with simultaneous flash separation of OA (see flowsheet in Figure S1), requiring much less NH_3 in excess and much lower pressure than in the batch reactor. At the beginning of the reaction, OL (1 kg) and Ru/HBEA(25)_4 (80 g) were loaded into the reactor under stirring (1000 rpm). The catalyst was then activated using H_2 pulses by switching the H_2 pressure from 0.4 barg to 1.0 barg at 180 °C for 30 s at a flowrate of 6 L(STP)/min. Keeping the H_2 pressure at 1.0 barg to avoid ON formation, NH_3 was loaded until a maximum pressure of 4.5 barg, and the reactor was first operated in semi-batch mode for 10 h by setting the gas circulation loop pump at 2.5 L(STP)/min. After this period, the reactor was operated in continuous mode by feeding OL at 25 g/h and NH_3 at a NH_3 partial pressure of 4.5 barg, and keeping the H_2 pressure at 1.0 barg using pulses every 30 s. The vapor phase was simultaneously removed using a loop pump, followed by cooling in a heat exchanger cooler with ambient air and flash separation in a condenser. The organic phase enriched in OA and water was recovered from the bottom of the condenser, whereas NH_3 and H_2 were recovered from the top of the condenser and recirculated to the reactor through a sparger. A sampling pipe at the reactor bottom was used to take liquid samples during the reaction for monitoring the

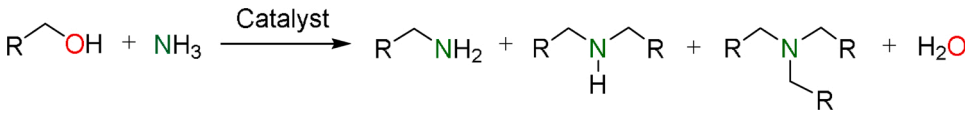

Scheme 1. Potential amination products in the direct amination reaction of OL with NH_3.

reactor composition.

The steady-state OL conversion (limiting reactant) and the selectivity to the N-containing products were defined as follows:

$$\text{Conversion}\ (\%) = 1 - \frac{F^{C}_{OL}}{F^{R}_{OL,0}} \tag{7}$$

$$\text{Selectivity}_{i}\ (\%) = \frac{F^{C}_{i}}{F^{R}_{OL,0} - F^{C}_{OL}} \quad i = 1 \ldots N - \text{products} \tag{8}$$

where $F^{R}_{OL,0}$ and F^{C}_{OL} are the molar flowrate of OL at the inlet of the reactor and at the outlet of the condenser, respectively, whereas and F^{C}_{i} corresponds to the molar flowrate of N-containing products at the outlet of the condenser.

3. Results and discussion

3.1. Catalytic activity of Ru catalysts

In a first series of experiments, we explored the effect of the Ru particle size on the catalytic activity for OA formation (TOF_{OA}) for a series of Ru-loaded catalysts over a variety of supports (Fig. 1). For comparison, the catalytic activity was also measured on Ru black. Table 1 lists the main properties of the catalysts. In the experiments, the nominal NH_3/OL molar ratio was kept in the range 5–15 to favor OA formation (Figure S2).

Irrespective of the particle size, the catalytic activity over Ru black and Ru/C keeps almost unchanged with the average size of Ru nanoparticles at a value about 30 h^{-1}. This observation agrees well with two recent studies on unsupported Ru nanoparticles stabilized with CTAB (*ca.* 2−9 nm) and Ru/TiO_2, where the catalytic activity for OL amination with NH_3 was found to be insensitive to the size of Ru nanoparticles [25, 44]. Nonetheless, the catalytic activity exhibits a neat enhancement when the Ru particles are loaded over acid supports with a TOF_{OA} of about 100 h^{-1}, which is especially visible for Ru/HBEA(25) [Ru size =17 nm, i.e. Ru/HBEA(25)_4, Table 1], Ru/ZSM-5(20), Ru/HY(10), Ru/SiO_2, Ru/Al_2O_3 and Ru/MgO.

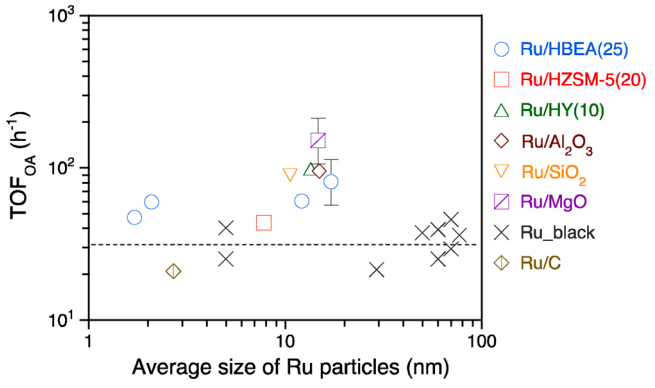

Fig. 1. Evolution of TOF_{OA} as a function of the average size of Ru NPs for supported Ru catalysts and Ru black for OL amination with NH_3. Reaction conditions: OL- 6.3 mmol, NH_3/OL- 15, H_2- 5 bar, T- 180 °C, Cat- 120-250 mg for supported Ru catalysts (0.19-3.1 mol% Ru with respect to OL) and 15.1-45.6 mg for Ru black (0.010-1.7 mol% Ru with respect to OL), rpm- 600. The reaction time was adjusted to achieve 10-20 % OL conversion. The catalysts were pre-reduced before the catalytic tests.

Table 1
Main properties of the different Ru catalysts prepared in this study.

Entry	Catalyst	Ru loading (wt%) [a]	S_{BET} (m^2/g) [b]	S_{ext} (m^2/g) [b]	V_g (cm^3/g) [b]	$\bar{d}_{p,Ru}$ (nm) [c]
1	Ru/HZSM-5(30)	5.5	376	85	0.17	7.8
2	Ru/HY	6.6	690	105	0.31	13.5
3	Ru/Al_2O_3	7.5	139	139	0.21	14.9
4	Ru/SiO_2	3.7	187	190	0.20	10.6
5	Ru/MgO	3.4	39	34	0.17	14.9
6	Ru/C	3.9	782	334	0.14	2.7
7	Ru/HBEA (25)_1	0.16	–	–	–	1.7[d]
8	Ru/HBEA (25)_2	0.43	–	–	–	2.1[d]
9	Ru/HBEA (25)_3	1.0	373	170	0.60	17.0
10	Ru/HBEA (25)_4	5.0	530	156	0.29	17.1
11	Ru/HBEA (25)_5	9.6	498	142	0.26	12.1
12	Ru/ 1NaBEA (25)_4	5.0	533	158	0.29	17.0
13	Ru/ 2NaBEA (25)_4	5.0	548	155	0.28	17.0
14	Ru/HBEA (150)	4.6	628	177	0.32	16.1
15	Ru/HBEA (300)	4.8	–	–	0.31	14.2
16	HBEA(25)	–	563	136	0.32	–

[a] Measured by XRF and H_2-TPR on the calcined catalysts.
[b] Measured by N_2 adsorption at −196 °C.
[c] Measured by XRD (Scherrer equation) including density correction.
[d] Measured by HR-TEM and pulsed CO chemisorption.

Overall, these results suggest that the acidity is a key factor governing the activity for the series of catalysts tested, but not the Ru particle size.

3.2. Selectivity vs. Conversion curves

We further investigated the selectivity of the Ru catalysts as a function of the OL conversion at comparable Ru loading (Fig. 2). In all cases, the OA selectivity exhibits a decreasing trend with the OL conversion at the expense of DOA, whereas only traces of TOA and ON are detected. Nonetheless, four selectivity-conversion patterns can be discerned. First, Ru black (Ru size =5 nm) (back curve) displays a moderate decline of the OA selectivity until 30 % and 45 % OL conversion, followed by a sharp decrease until an OA selectivity of 65 % at 60 % OL conversion. Second, Ru/C (Ru size =2.6 nm) (green curve) also displays a moderate decline of the OA selectivity until 30 % OL conversion, followed by a prominent decline of the OA selectivity, even if softer, until 70 % at 90 % OL conversion. Third, Ru/ZSM-5(20) (Ru size =7.8 nm), Ru/HY(10) (Ru size =13 nm), Ru/Al_2O_3 (Ru size =15 nm) Ru/SiO_2 (Ru size =10.6 nm) and MgO (Ru size =11 nm) (red curves) show a monotonous decrease of the OA selectivity, reaching a value of 85 % at 80 % OL conversion. Finally, Ru/BEA(25)_4 (Ru size =17 nm) (blue curve) exhibits only a slight decline of the OA selectivity to 90 % at 90 % OL conversion, resulting in a OA yield of 81 %. To our knowledge, this is the highest ever-reported yield on metal-supported catalysts for OL amination,

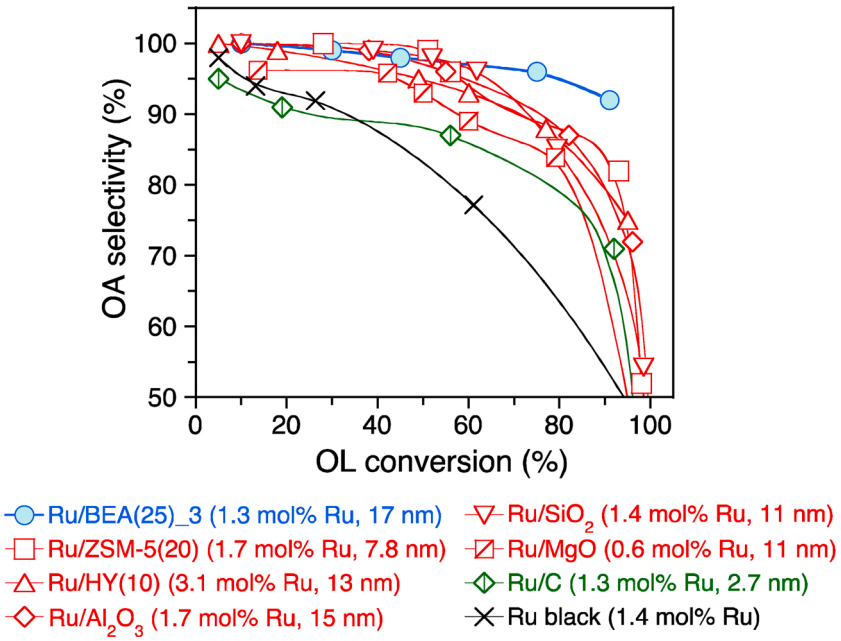

Fig. 2. Selectivity – conversion curves for OL amination with NH_3 over the different Ru catalysts at comparable Ru loading. Reaction conditions: OL- 6.3 mmol, NH_3/OL- 15, H_2- 5 bar, T- 180 °C, Cat- 110-250 mg for supported catalysts and 9.0 mg for Ru black, rpm- 600. The catalysts were pre-reduced before the catalytic tests. The carbon balance was in the range 5-10 % for the different tests.

overcoming the value achieved on NiPd/Al_2O_3 (5 wt% Ni, 0.5 wt% Pd) (71 %) prepared in the presence of β-CD [45].

Given the high OA selectivity and yield obtained on Ru/BEA(25)_4, we further measured the selectivity-conversion curve on Ru/BEA(25)_4 as a function of the Ru loading in the reactor (Fig. 3). A Ru loading higher than 1.30 mol% Ru with respect to OL is enough to reach an OA selectivity higher than 90 % at 90 % OL conversion (blue curve). A decrease of the Ru loading down to 0.19 mol% Ru while keeping the average particle size unchanged at 17 nm [i.e. Ru/HBEA(25)_3] results in a remarkable decline of the OA selectivity (black curve), with a trend approaching that of the third pattern depicted in Fig. 2 for Ru/ZSM-5 (20), Ru/HY(10), Ru/Al_2O_3, Ru/SiO_2 and Ru/MgO.

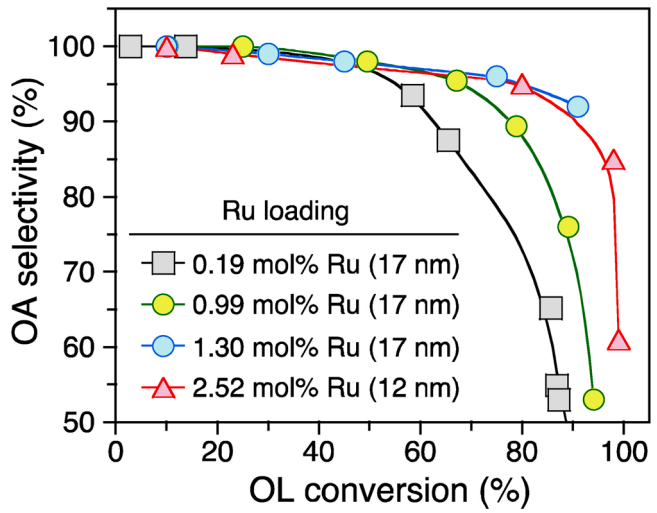

Fig. 3. Selectivity – conversion curves for OL amination with NH_3 over Ru/HBEA(25)_3 (squares), Ru/HBEA(25)_4 (circles) and Ru/HBEA(25)_5 (triangles) at variable Ru loading and comparable average size of Ru nanoparticles. Reaction conditions: OL- 6.3 mmol, NH_3/OL- 15, H_2- 5 bar, T- 180 °C, rpm- 600. The catalysts were pre-reduced before the catalytic tests. The carbon balance was in the range 5-10 % for the different tests.

3.3. *Effect of the acidity on the catalytic properties of Ru/HBEA*

To gain more insight into the effect of the acidity on the selectivity of Ru/HBEA(25)_4, we conducted a series of catalytic tests on Na-exchanged Ru/HBEA(25) catalysts (5 wt% Ru) (Fig. 4A). Two catalysts were prepared, i.e. Ru/1NaBEA(25)_4 and Ru/2NaBEA(25)_4, referring to one and two ion-exchange steps, respectively, resulting in an exchange of 1/3 and 2/3 of the acidity (H^+), respectively, as inferred by NH_3-TPD (Figure S3A-C). Compared to Ru/HBEA(25)_4, Ru/1NaBEA (25)_4 displays a decline of the OA selectivity from 92 % to 77 % at the expense of DOA at an OL conversion higher than 90 %. Further ion exchange to Ru/2NaBEA(25)_4 intensifies even more the decrease of the OA selectivity down to 60 % at the expense of DOA and ON, with a selectivity of 8% and 32 %, respectively, and encompasses a pronounced decrease of the OL conversion down to 41 %.

We also carried out a series of catalytic tests over Ru/HBEA(x) catalysts (5 wt% Ru) with variable Si/Al molar ratio (x), with $x = 20$, 150 and 300 (Fig. 4B). The corresponding NH_3-TPD profiles are plotted in Figure S3D-E. An increase of the Si/Al ratio from 20 to 150 results only in a moderate decrease of the OA selectivity from 92 % to 82 % at the expense of DOA while keeping the OL conversion at *ca.* 90 %. However, a further increase of the Si/Al ratio to 300 results in a marked decline of the OA selectivity down to 72 % in favor of DOA and ON, with a selectivity of 10 % and 27 %, respectively, encompassing also a pronounced decrease of the OL conversion down to 25 %.

Finally, we compared the catalytic performance of Ru/HBEA(25)_4 (5 wt% Ru) with that of a mechanical mixture of Ru black and the parent HBEA(25) at comparable Ru loading and particle size of Ru particles (Figure S4). The results show that Ru/HBEA(25)_4 outperforms the mechanical mixture both in terms of OL conversion and OA selectivity, confirming the synergistic role between Ru nanoparticles and acid centers in Ru/HBEA(25)_4.

3.4. *Stability tests in CSTR*

A catalytic test was carried out in a CSTR for assessing the stability of Ru/HBEA(25)_4 during continuous operation. Figure S5 plots the evolution of the composition in the condenser stream and reactor during

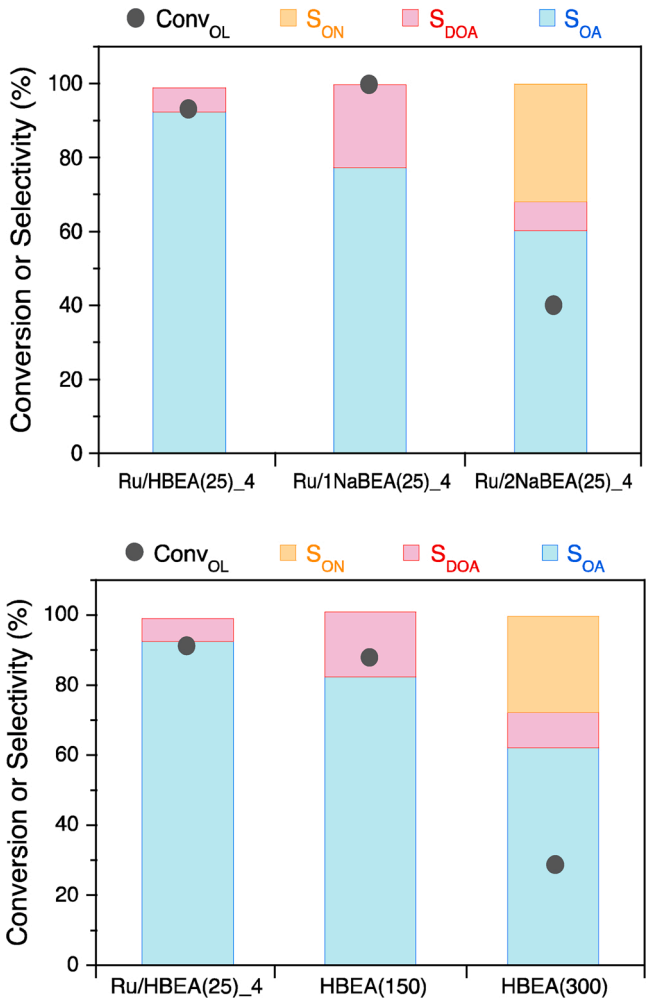

Fig. 4. On top, catalytic performance of Ru/BEA(25)_4 at different H^+-exchange degrees in the direct amination reaction of OL with NH_3; on bottom, catalytic performance of Ru/BEA (x) as a function of Si/Al ratio (x) with x = 20, 150 and 200. Reaction conditions: OL- 6.3 mmol, NH_3/OL- 15, H_2- 5 bar, T- 180 °C, Time- 16 h, Cat- 250 mg (1.5-2.0 mol%Ru with respect to OL), rpm- 600. The catalysts were pre-reduced before the catalytic tests. The carbon balance was in the range 5-10 % for the different tests. The acidity in the catalysts was measured by NH_3-TPD (Figure S3, Table S1).

120-h operation. After catalyst activation, the reactor was operated in semi-batch mode during 10 h (A), followed by continuous operation at 25 g/h with the temperature in the heat exchanger set at 150 °C (B), evolving from 150 °C to 90 °C (B), and set at 90 °C (C). During the first step (A), the DOA concentration in the reactor increases to a value up to 58.5 wt%. After this period, the reactor was switched to continuous mode at a flowrate of 25 g/h with concomitant removal of OA out of the reactor. The temperature in the heat exchanger was first set at 150 °C during 70 h (B), and was then decreased from 150 °C to 90 °C for the next 50 h (C). The reactor composition keeps relatively stable at steady state with 3.8 wt% OL, 2.7 wt% OA, 38 wt% DOA and 55 wt% TOA (Fig. 5). Two liquid phases were recovered from the condenser, i.e. the organic and aqueous phases. The mass balance calculated by GC analysis is around 0.92 ± 0.02 for the organic phase, which matches the water content in the aqueous phase (7.0 ± 0.5 wt%) measured by Karl Fischer titration in steady state. The OA composition in the organic phase reaches 80 % with 87 % OL conversion when the condenser is operated at 90 °C.

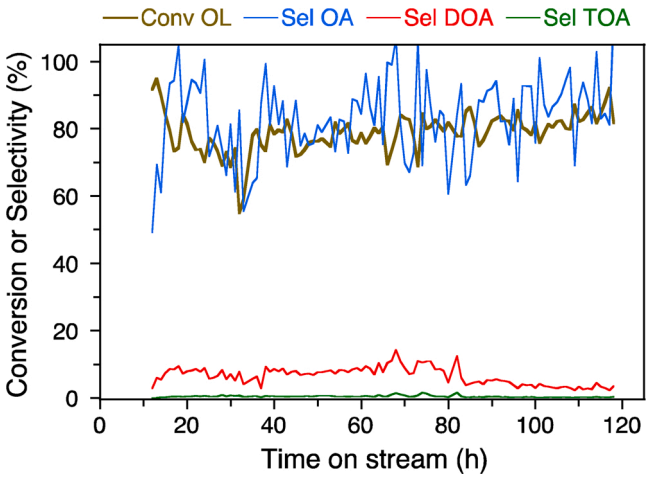

Fig. 5. Time-evolution of the OL conversion and selectivity to the different amines during continuous OL amination with NH_3 in CSTR (operation mode C in Figure S5). Reaction conditions: OL flowrate 25 g/h, NH_3- 4.5 barg, H_2- 1.0 barg, T- 180 °C, WHSV- 0.3 h^{-1}. The catalysts were pre-reduced before the catalytic tests.

3.5. *Characterization of Ru/HBEA(25)_4*

The catalytic results for OL amination presented above point out an enhanced activity and OA selectivity for Ru/HBEA(25)_4. In light of these results, we explored in detail the structure of Ru/HBEA(25)_4 among the different Ru-supported catalysts prepared in this study, and its evolution during the amination reaction.

3.5.1. *Textural properties*

N_2 adsorption/desorption at 77 K was carried out to characterize the surface area and pore volume of the different catalysts. Table 1 compiles the textural properties of the catalysts. The different Ru/H-BEA catalysts display a Type I adsorption pattern with a hysteresis loop at P/P_0 from 0.6 to 1 reflecting the simultaneous presence of micropores and mesopores. The specific surface area decreases from 563 m^2/g for the parent HBEA(25) to 530 m^2/g for Ru/HBEA(25)_4, whereas the pore volume only declines slightly from 0.32 cm^3/g to 0.29 cm^3/g. This set of results suggests that most of Ru is loaded in the form of nanoparticles being located at the external surface of H-BEA(25).

3.5.2. *Crystal structure of Ru nanoparticles*

The structure of Ru/HBEA(25)_4 was inspected by PXRD before and after reduction (Figure S6a-c). The catalyst displays reflections at 28°, 35°, 40° and 54° in addition to those belonging to the parent HBEA(25), being ascribed to the (110), (101), (200) and (211) planes of RuO_2, respectively. Two new reflections appear at 38° and 44° in the reduced samples, which can be assigned to the (100) and (101) planes of metal Ru. The RuO_2 and Ru average particle size ranges from 7 to 15 nm as inferred by the Scherrer equation applied to reflections (110) for RuO_2 and (101) for Ru, respectively (Table 1). Ru/HBEA(25)_4 was also inspected by HR-TEM to measure the distribution of Ru nanoparticles. The average size of Ru nanoparticles is about 17 nm (Fig. 6b,c), being compatible with the range measured from PXRD. For comparison, Ru/C with Ru particles <1 nm as measured by HR-TEM do not show reflections in the corresponding PXRD patterns (Fig. 6d).

XPS analysis was conducted to gain more insight into the surface state of the Ru species on Ru/HBEA(25)_4 before reduction (Table S2, S3). Ru exhibits two spin-orbital coupled bands for the Ru 3d core level that can be deconvoluted into 3 and 4 bands, respectively. The main bands at 280.8 eV and 283.8 eV can be assigned to RuO_2 (Figure S7a) [46–49]. Two additional bands centered at 282.7 eV and 286.6 eV with a relative intensity about 1:1 can also be discerned, which are attributed

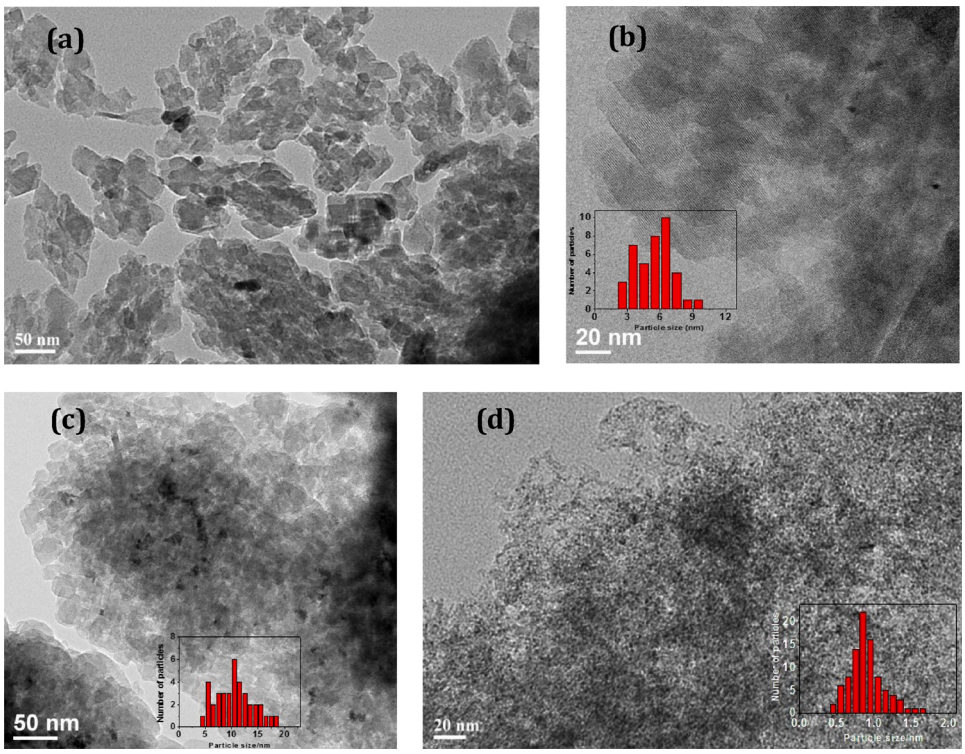

Fig. 6. HR-TEM micrographs of (a) H-BEA(25), (b-c) Ru/H-BEA(25)_4 and (d) Ru/AC.

to partially hydrated RuO_2 (i.e. $RuO_2 \cdot nH_2O$) [50,51]. The Ru 3p core level is also splitted in two spin-orbital coupled bands, which can be each deconvoluted in two bands corresponding to RuO_2 (462.6 / 485.2 eV) and $RuO_2.nH_2O$ (466.1 / 488.2 eV), respectively (Figure S7b). Both species are also predominant on the spent Ru/HBEA(25)_4 after reaction and calcination at 400 °C.

3.5.3. *Catalyst reducibility*

The reducibility of RuO_2 species in Ru/H-BEA(25)_4, Ru/ZSM5, Ru/HY, Ru/Al_2O_3 and Ru/SiO_2 before reduction was studied by H_2-TPR (Figure S8). A symmetric band centered at 150 °C is visible for Ru/SiO_2, reflecting the presence of homogeneous RuO_2 species. In contrast, for Ru/H-BEA(25)_4, Ru/HZSM5(20), Ru/HY(10) and Ru/Al_2O_3, the reduction of RuO_2 species is splitted into different bands appearing in the range 90−200 °C, pointing out a stronger interaction between RuO_2 nanoparticles and the acid support. The lack of reduction bands at higher temperature suggests the absence of Ru^+ species in the zeolite channels. Opposing this behavior, an additional band appears on Ru/HY (10) by 450 °C, which might be attributed to the reduction of small RuO_2 nanoparticles or isolated metal sites inside the HY cavities.

The reducibility of RuO_2 species in Ru/H-BEA(25)_4 could be also visualized by NH_3-TPD (Figure S9). Indeed, the NH_3-TPD profile of the unreduced sample, i.e. RuO_2/HBEA(25)_4, is characterized by a band centered at 340 °C that is attributed to the desorption of N_2 upon reduction by NH_3.

3.5.4. *Evolution of the local atomic and electronic structure of Ru-species*

A dedicated XAS study of Ru/HBEA(25)_4 was carried out to assess

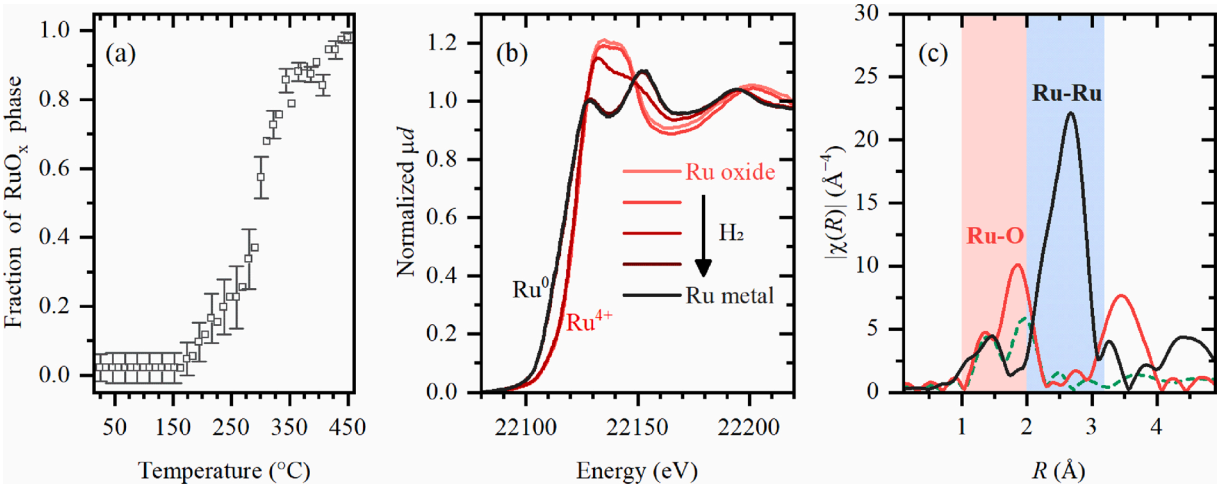

Fig. 7. (a) Fraction of RuO_x phase estimated from a linear combination fit of the XANES spectra along the formation of RuO_x particles from $RuCl_3$ precursor in 20 % O_2/He from RT to 450 °C. (b) Formation of Ru nanoparticles (from light red to black) under H_2 at 180 °C as a function of time followed by Ru *K*-edge XANES. (c) Fourier-transformed EXAFS spectra for initial sample (dashed green), after oxidation (red) and after successive reduction (black).

the microenvironment around Ru-sites. *In situ* XAS spectra were collected during calcination and pre-reduction of the catalyst, and during the amination reaction of OL with NH_3. Fig. 7a shows the evolution of ruthenium oxide during the calcination step. $RuCl_3$ starts to generate the oxide at around 185 °C and the formation is accelerated at a temperature higher than 290 °C. At 450 °C, almost all the Ru precursor is converted into the oxide. The RuO_x/HBEA(25) sample is completely reduced *in situ* under H_2 at 180 °C for 30 min (Fig. 7b). No evidence of residual RuO_x species is observed, as well as the formation of a metal hydride phase (Ru-H).

The first-shell analysis of the EXAFS spectra confirms the formation of ruthenium oxide particles and their complete reduction to metal ruthenium (Fig. 7c). To estimate the average size of Ru nanoparticles, the Ru-Ru first-shell coordination number, *N*, was considered. For the particles after reduction at 180 °C under H_2, the coordination number is 11 ± 0.8, which corresponds to an average particle size in the range 3−20 nm in agreement with the sizes measured by PXRD (Figure S6c) and HR-TEM (Fig. 6). In light of these results, Ru nanoparticles are expected to be located at the external surface of HBEA(25), which is also consistent with the low-temperature reduction profile of Ru/HBEA(25)_4.

The reduced Ru/HBEA(25)_4 was further monitored under reaction conditions in the presence of NH_3 and 1-hexanol in the gas phase. Although the EXAFS spectra are dominated by Ru-Ru scattering, which remains stable along the reaction, changes in the electronic structure of Ru affect the shape of XANES spectra, making them sensitive to the presence of light impurities on Ru nanoparticles, such as carbon, nitrogen or hydrogen species [52]. Initially, solely NH_3 was sent through the sample, which induces an increase of the first XANES maximum at *ca.* 22,128 eV towards higher energies, and the shift of the second maximum at *ca.* 22,152 eV towards lower energies (Fig. 8a, blue curve). A similar trend is observed in *ab initio* simulations performed with the finite difference method (FDMNES) code for pure Ru surface (Fig. 8b, solid black curve) [53], and for a surface atom with on-top N-atom (Fig. 8b, dashed blue curve), which reveals that N-containing species are present at the surface of Ru nanoparticles. Upon successive interaction with 1-hexanol, the XANES spectrum partially reverts to the initial activated state, indicating that N-containing species react with the alcohol. The later fact was proved by online MS monitoring of $m/Z = 30$ signal corresponding to 1-hexylamine as shown in Figure S10.

3.5.5. Acidity of the catalysts

3.5.5.1. NH_3-TPD profiles. NH_3-TPD was employed to characterize the distribution and strength of acid sites on the different catalysts (Fig. 9, Table S4). The acid site strength can be broadly classified in three main groups after deconvolution: (1) weak acid sites and $NH_4^+ \cdot nNH_3$

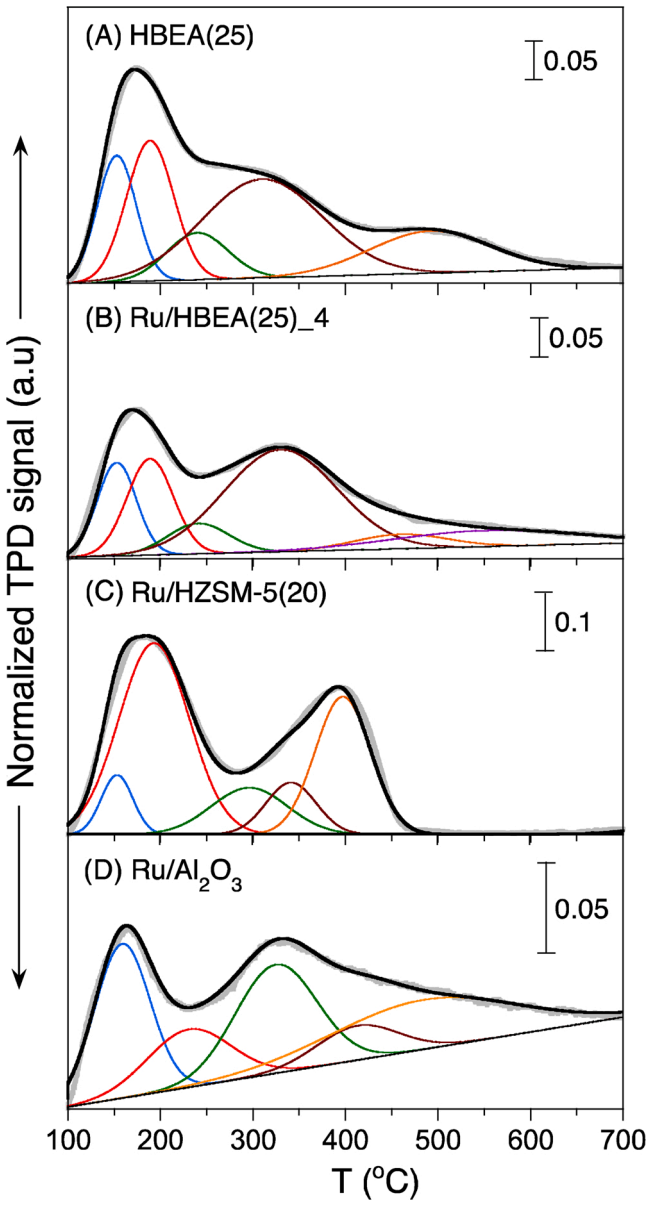

Fig. 9. NH_3-TPD profiles of (A) HBEA(25), (B) Ru/HBEA(25)_4, (C) 5Ru/HZSM-5(20) and (D) 5Ru/Al_2O_3.

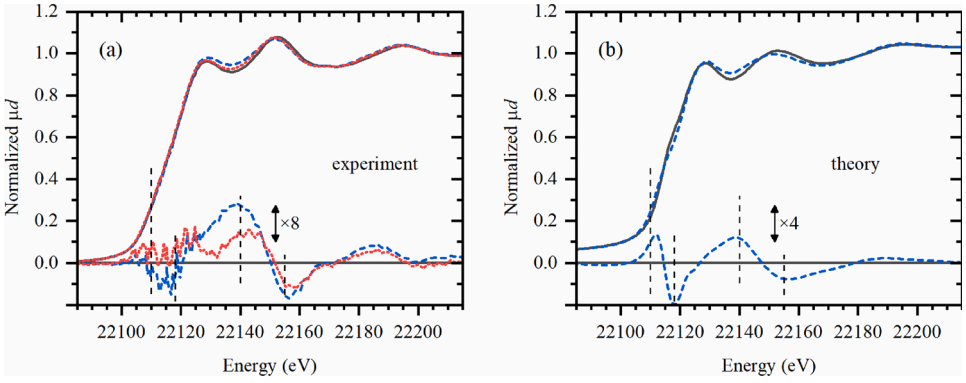

Fig. 8. (a) Experimental Ru *K*-edge XANES collected at 180 °C for reduced Ru/HBEA(25)_4 in inert atmosphere (solid black), under NH_3 flow (dashed blue) and under a flow of NH_3 and 1-hexanol (dotted red). The difference spectra are shown in increased vertical scale to highlight the changes induced by different atmospheres. (b) Theoretical XANES spectra for surface Ru atom at pure (102) surface (solid black) and the same atom but with on-top N-atom (dashed blue).

associations promoted by H-bonding (100−400 °C, bands I–V), (2) medium acid sites (400−550 °C, bands VI and VII), and (3) strong acid sites between (550−900 °C, bands VIII and IX).

The NH_3-TPD profiles were first measured and deconvoluted for HBEA(25). Four bands are observed corresponding to sites with weak (bands I—IV) and medium (band VII) acid strength. The density of acid sites excluding bands I and II (563 μmol.g^{-1}), which are attributed to NH_4^+.nNH_3 associations, is compatible with the Si/Al molar ratio (25) given the molecular formula of HBEA [$H_xSi_{64-x}Al_xO_{128}$] [54]. The NH_3 desorption pattern keeps almost unchanged for pre-reduced Ru/HBEA (25)_4, but band IV shifts slightly to higher temperature (from 310 °C to 330 °C), and band VII splits into two bands, i.e. bands VII and VIII, centered at 460 °C and 555 °C, respectively. The density of acid sites excluding bands I and II (480 μmol.g^{-1}) exhibits a decline compared to the parent HBEA(25) (563 μmol.g^{-1}), suggesting partial removal of acid sites on the external surface during Ru reduction. The density of acid sites attributed to band II decreases from 188 μmol.g^{-1} in HBEA(25) to 121 μmol.g^{-1} in Ru/HBEA(25)_4. This observation reinforces the idea of a preferential location of Ru nanoparticles on the external surface of HBEA(25), rendering the support slightly less hydrophilic.

The NH_3-TPD profile of Ru/HZSM-5(20) comprises 6 bands corresponding to sites with weak (bands I–V) and strong acid strength (bands VII-IX). Noteworthy, no bands in the medium acid strength region are observed. The total density of acid sites is 626 μmol.g^{-1} excluding bands I and II. Bands II and VI exhibit the highest intensity with a density of acid sites of 454 μmol.g^{-1} and 260 μmol.g^{-1}, respectively, while bands IV, V and IX show a density of 120, 88 and 158 μmol.g^{-1}, respectively. The NH_3-TPD profile of Ru/Al_2O_3 is constituted of 5 bands corresponding to sites with weak (band III) and medium acid strength (bands IV, VI, VII). The total density of acid sites is 244 μmol.g^{-1} excluding band I (no band II is present). Bands IV and VI show a density of acid sites of 105 and 106 μmol.g^{-1}, respectively, which is slightly lower than the density measured on Ru/HBEA(25)_4 for band V-VII (144 μmol.g^{-1}). Finally, the NH_3-TPD profile on Ru/SiO_2 (not shown) only exhibits weak desorption bands in the low-temperature region, which can be attributed to the low acid strength of SiO_2.

3.5.5.2. OA-TPD profiles. To gain more insight into the acidity of the different catalysts, we measured the OA-TPD profiles on the different supports (Fig. 10, Table S5). Overall, two main regions can be distinguished: (1) low-temperature region (100−300 °C, bands II—V), and (2) high-temperature region (300−500 °C, bands V-VIII). The first region can be attributed to OA physisorption or adsorption on acid sites at the external surface, whereas the second region can be ascribed to OA adsorption in the zeolite channels.

The OA-TPD profile was first measured and deconvoluted for HBEA (25). Four bands can be clearly visualized in the first region with an overall OA density of 362 μmol.g^{-1}. The second region also comprises four bands with an overall OA density of 677 μmol.g^{-1}, which compares well with the total acid density measured by NH_3-TPD (740 μmol.g^{-1}). The latter observation points out an efficient packing of OA in the BEA channels, which was confirmed by DFT modeling (not shown). The OA-TPD profile on HZSM-5(20) exhibits a similar pattern, but with two differences compared to the profile on HBEA(25). First, the density of OA desorbed in the low-temperature region is much lower (76 μmol.g^{-1} *vs.* 362 μmol.g^{-1}). Second, the bands appearing in the high-temperature region are shifted to lower temperature and encompass an OA density of 574 μmol.g^{-1}, which is much lower than the total acidity in HZSM-5 measured by NH_3-TPD, pointing out a less efficient packing of OA in the ZSM-5 channels.

We also measured the OA-TPD profiles on Al_2O_3 and SiO_2. On the one hand, the OA-TPD profile on Al_2O_3 shows bands belonging to the two regions with an overall density of 168 μmol.g^{-1} and 128 μmol.g^{-1}, respectively. Unlike HBEA(25) and ZSM-5(20), the much lower OA density in the high-temperature region is attributed to the lack of microporosity in Al_2O_3. On the other hand, the OA-TPD profile on SiO_2 only exhibits bands in the low-temperature region (range 100−200 °C) with a total OA density of 571 μmol.g^{-1}.

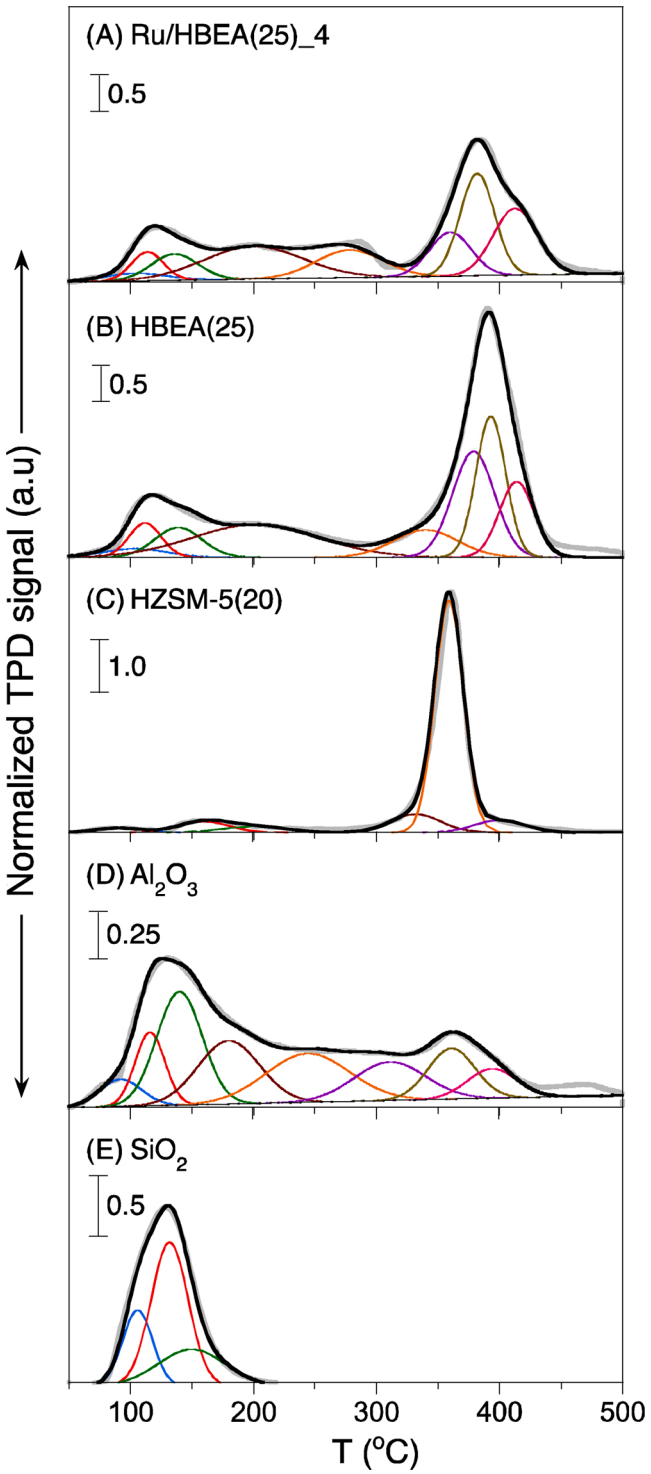

Fig. 10. OA-TPD profiles of (A) Ru/HBEA(25)_4, (B) HBEA(25), (C) HZSM-5 (20), (D) Al_2O_3 and (E) SiO_2.

Overall, the results above point out a higher ability of HBEA(25) and Ru/HBEA(25)_4 for desorbing OA at a temperature near 180 °C, which corresponds to the reaction temperature for OL amination with NH_3. This property combined with the medium strength of the acid sites, affording a pre-concentration near the Ru nanoparticles, are regarded as key drivers for the selectivity towards OA in Ru/HBEA(25)_4.

3.5.5.3. ^{27}Al MAS NMR spectra. ^{27}Al MAS NMR was used to complete our understanding on the nature of acid sites in the calcined HBEA(25) and Ru/HBEA(25)_4 (Figure S11, Table S6). The spectra consist of two main resonance bands centered at about 55 pm and 0 ppm. The first band can be deconvoluted into 3 elementary bands centered at 58.1, 53.0 and 47.6 ppm for HBEA(25) and 59.5, 53.2 and 43.0 ppm for HBEA (25) matching earlier observations [55]. These bands are indicative of fourfold (^{IV}Al) coordinated species in the zeolite framework generating Si-O(H)-Al Brønsted acid sites. The difference between the three sites can be attributed to a small change in the T-O-T angles (T = Si or Al), i.e. the higher the T-O-T angle, the more negative is the chemical shift for Al [56]. An addition band is observed at 23.0 ppm for Ru/HBEA(25)_4 that is not visible in HBEA(25) and that can be assigned to fivefold (^{V}Al) species. This site is attributed to extra-framework $Al(OH)_2^+$ or Al^{n+} species tightly coordinated with framework oxygen atoms, exhibiting Lewis acidity [57].

The second main band at about 0 ppm is generally attributed to sixfold (octahedrally) coordinated Al sites in partially hydrated zeolites. This band can be deconvoluted into 4 elementary bands centered at 3.8, -0.1, -7.5 and -19.0 ppm for HBEA(25) and 4.0, 0.0, -7.9 and -21.5 ppm for Ru/HBEA(25)_4. Hu and co-workers [58] have recently attributed the former two bands to extra-framework hydrated $Al(OH)_3$ (3.8 ppm) and $Al(H_2O)_6^{3+}$ (*ca.* 0 ppm) in a high symmetrically coordinated environment, respectively, whereas the third band (-7.5 ppm) has been ascribed to framework Al species in an asymmetrically coordinated environment. The fourth band can be attributed to extra-framework alumina-type phases located either in the pores or on the external surface [59]. All these species, partially dehydrated, can behave as Lewis acid centers. Finally, the presence of NMR-invisible Al species associated to transient states, cannot be ruled out [60]. The incorporation of Ru over HBEA(25) results in an increase of sixfold-coordinated species (Lewis acid centers) compared to the parent HBEA(25), as can be inferred from a higher Lewis-to-Brønsted acid ratio, i.e. (^{V}Al + ^{VI}Al) / ^{IV}Al, in the former sample (0.28 vs. 0.70). This observation suggests that bands IV and VII in the deconvoluted NH_3-TPD profile of HBEA(25) (Fig. 10A, Table S4 – entry 1) correspond to Lewis acid species, which shift to higher temperature in the presence of ruthenium in Ru/HBEA (25)_2 (Fig. 10C, Table S4 – entry 3).

For comparison, we measured the ^{27}Al MAS NMR spectra on HBEA (150) and Ru/HBEA(150) (Figure S12, Table S6). Compared to HBEA (25) and Ru/HBEA(25)_4, the band at about 0 ppm exhibits much lower surface, pointing out a much lower density of sixfold coordinated Al species. Indeed, the Lewis-to-Brønsted acid ratio, i.e. (^{V}Al + ^{VI}Al) / ^{IV}Al, in both samples is about 0.045. The band centered at 55 ppm can be deconvoluted into 5 bands, including a band centered at about 60 ppm that is not observed on HBEA(25) and Ru/HBEA(25)_4. Besides, the band centered at 0 ppm can be deconvoluted into 3 bands without the presence of a band by -19 ppm being attributed to alumina species.

Overall, these results point out potential dealumination in HBEA(25) during Ru impregnation, resulting most likely in the generation of AlO_x clusters on the external surface stabilizing the Ru nanoparticles. In contrast, in the case of HBEA(150) with much lower Al content, almost no dealumination is observed. Accordingly, in the former case, Ru@A-lO_x on the external surface of HBEA(25), with Lewis acidity, could behave as active sites for the reaction, where the internal Brønsted centers could behave as NH_3 storage buffer.

4. Conclusion

A Ru/HBEA (Si/Al = 25) catalyst with 5 wt% Ru exhibited high selectivity to the primary amine (>90 %) at high conversion (>90 %) in the direct amination reaction of 1-octanol with ammonia at 180 °C in a batch reactor. The catalyst was further tested in a continuous stirred-tank reactor (2 L) with flash separation of octylamine. In this configuration, 92 % selectivity of octylamine was obtained at 87 % 1-octanol conversion during 120 h on steam. The high catalytic performance was attributed to the location of Ru nanoparticles (17 nm) on the external surface of HBEA surrounded by Brønsted / Lewis acid centers with medium strength, as inferred by combining XRD, BET, HR-TEM, NH_3-TPD, OA-TPD, H_2-TPR, XPS, EXAFS/XANES, ^{27}Al MAS NMR and TGA. This surface architecture promotes the pre-concentration and reactivity of NH_3 near the metallic Ru nanoparticles, as well as fast desorption of 1-octylamine at the reaction temperature.

Supporting Information

XRD patterns of fresh HBEA(25), fresh RuO_2/HBEA(25)_4, reduced Ru/HBEA(25)_4 and spent Ru/HBEA(25)_4; deconvoluted XPS spectra of the Ru 3p and Ru 3d core levels for the fresh / unreduced and spent / calcined (400 °C) Ru/HBEA(25)_4; deconvoluted NH_3-TPD profiles of HBEA(25), 1NaHBEA(25), 2NaHBEA(25), HBEA(150), HBEA(300) and RuO_2/HBEA(25)_4; results for band deconvolution of OA-TPD profiles for RuO_2/HBEA(25)_4, HBEA(25), HZSM-5(20), Al_2O_3 and SiO_2; H_2-TPR profiles of Ru/HBEA(25)_4, Ru/HZSM-5(20), Ru/HY(10), Ru/Al_2O_3 and Ru/SiO_2.m/z = 30 signal corresponding to 1-hexylamine collected during *in situ* XAS measurements by online MS; ^{27}Al NMR MAS spectra on HBEA(25), Ru/HBEA(25)_4, HBEA(150) and Ru/HBEA(150), and results for band deconvolution; flowsheet of the setup used for catalytic tests in CSTR with simultaneous OA separation; OL amination results with NH_3 over Ru/HBEA(25)_4 as a function of the NH_3/OL ratio; catalytic performance of Ru/HBEA(25)_4 and a physical mixture of Ru black and HBEA(25); time-evolution of the composition in the condenser stream (top) and reactor (bottom) during OL amination with NH_3 in CSTR.

CRediT authorship contribution statement

L. Fang: Conceptualization, Methodology. **Z. Yan:** Project administration. **J. Wu:** Investigation. **A. Bugaev:** Investigation. **C. Lamberti:** Conceptualization. **M. Pera-Titus:** Conceptualization, Writing - original draft.

Declaration of Competing Interest

X The authors declare that they have no known competing financial interests or personal relationships that could have appeared to influence the work reported in this paper.

Acknowledgements

This work was supported by the French Agency of Research (ANR) through SHAPes program (contract 13-CDII-0004-06), the Science and Technology Commission of Shanghai Municipality (14301-412212-16017), and the Minhang District of Shanghai (2016MH177). A.B. acknowledges the Russian Science Foundation grant # 20-43-01015 for the funding the Ru K-edge XAS measurements and analyses, as well the President's Grant of the Russian Federation for Young Scientists MK-2554.2019.2 (agreement # 075-15-2019-1096) for travel support.

Appendix A. Supplementary data

Supplementary material related to this article can be found, in the online version, at doi:https://doi.org/10.1016/j.apcatb.2021.119942.

References

[1] H.A. Wittcoff, B.G. Reuben, J.S. Plotkin, Industrial Organic Chemicals, 2nd ed., Wiley, NY, 2004.
[2] S.A. Lawrence, Amines: Synthesis, Properties and Applications, Cambridge University Press, 2004.
[3] P. Roose, K. Eller, E. Henkes, R. Rossbacher, H. Höke, Aliphatic Amines, Ullmann's Encyclopedia of Industrial Chemistry, Wiley-VCH, Weinhein, 2002, pp. 1–55.

[4] K. Visek, Fatty Amines, Kirk-Othmer Encyclopedia of Chemical Technology, John Wiley & Sons, 2000.
[5] M. Pera-Titus, F. Shi, Chem. Sus. Chem. 7 (2014) 1–4.
[6] J. Pašek, P. Kondelik, P. Richter, Ind. Eng. Chem. Prod. Res. Dev. 11 (1972) 333–337.
[7] D.R. Corbin, S. Schwarz, G.C. Sonnichsen, Catal. Today 37 (2014) 71–102.
[8] G. Rice, E.J. Koh, J. Org. Chem. 77 (1955) 4052–4054.
[9] A. Mehta, A. Thaker, V. Londhe, S.R. Nandan, Appl. Catal. A Gen. 478 (2014) 241–251.
[10] K.-I. Shimizu, K. Kon, W. Onodera, H. Yamazaki, J.N. Kondo, ACS Catal. 3 (2013) 112–117.
[11] K.-I. Shimizu, Catal. Sci. Technol. 5 (2015) 1412–1427.
[12] A. Tomer, Z. Yan, A. Ponchel, M. Pera-Titus, J. Catal. 356 (2017) 133–146.
[13] J.V.M. de Pinillos, R.L. Fowlkes, US 4,314,084, 1982.
[14] J.H. Cho, J.H. Park, T.S. Chang, G. Seo, C.H. Shin, Appl. Catal. A Gen. 417-418 (2012) 313–319.
[15] D.M. Gardner, R.T. Clark, US 4,255,357, 1981.
[16] G.S. Sewell, C.T. O'Connor, E. van Steen, J. Catal. 167 (1997) 513–521.
[17] G.A. Vedage, L.A. Emig, H.-X. Li, J.N. Armor, US 5,917,092, 1998.
[18] A.K. Rausch, E. van Steen, F. Roessner, J. Catal. 253 (2008) 111–118.
[19] G. Liang, A. Wang, L. Li, G. Xu, N. Yang, T. Zhang, Angew. Chem. Int. Ed. 56 (2017) 3050–3054.
[20] T. Komanoya, T. Kinemura, Y. Kita, K. Kamata, M. Hara, J. Am. Chem. Soc. 139 (2017) 11493–11499.
[21] D. Chandra, Y. Inoue, M. Sasase, M. Kitano, A. Braumik, K. Kamata, H. Hisono, M. Hara, Chem. Sci. 9 (2018) 5949–5956.
[22] D. Deng, Y. Kita, K. Kamata, M. Hara, ACS Sust. Chem. Eng. 7 (2019) 4692–4698.
[23] K. Yamaguchi, J. He, T. Oishi, N. Mizuno, Chem. Eur. J. 16 (2010) 7199–7207.
[24] D. Ruiz, A. Aho, T. Saloranta, K. Eränen, J. Wärnå, R. Leino, D.Y. Murzin, Chem. Eng. J. 307 (2017) 739–749.
[25] G. Liang, Y. Zhou, J. Zhao, A.Y. Khodakov, V.V. Ordomsky, ACS Catal. 8 (2018) 11226–11234.
[26] C. Dong, H. Wang, H. Du, J. Peng, Y. Cai, S. Guo, J. Zhang, C. Samart, M. Ding, Mol. Catal. 482 (2020), 110755.
[27] X. Li, T. Guo, Q. Xia, X. Liu, Y. Wang, ACS Sust. Chem. Eng. 6 (2018) 4390–4399.
[28] C. Michel, P. Gallezot, ACS Catal. 5 (2015) 4130–4132.
[29] J.C. Siria, M. Duran, A. Lledos, J. Bertran, J. Am. Chem. Soc. 109 (1987) 7623–7629.
[30] E.S. Vasiliadou, E. Heracleous, I.A. Vasalos, A.A. Lemonidou, Appl. Catal. B: Environ. 92 (2009) 90–99.
[31] L. Corbel-Demailly, B.-K. Ly, D.-P. Minh, B. Tapin, C. Especel, F. Epron, A. Cabiac, E. Guillon, M. Besson, C. Pinel, Chem. Sus. Chem. 6 (2013) 2388–2395.
[32] J.-M. Lee, P.P. Upare, J.-S. Chang, Y.K. Hwang, J.H. Lee, D.W. Hwang, D.-Y. Hong, S.H. Lee, M.-G. Jeong, Y.D. Kim, Y.-U. Kwon, Chem. Sus. Chem 7 (2014) 2998–3001.
[33] Y. Wang, Z. Rong, Y. Wang, T. Wang, Q. Du, Y. Wang, J. Qu, ACS Sust. Chem. Eng. 5 (2017) 1538–1548.
[34] Z. Wu, S. Ge, C. Ren, M. Zhang, A. Yip, C. Xu, Green Chem. 14 (2012) 3336–3343.
[35] Y.-B. Huang, L. Yan, M.-Y. Chen, Q.-X. Guo, Y. Fu, Green Chem. 17 (2015) 3010–3017.
[36] N. Li, Y. Zheng, L. Wei, H. Teng, J. Zhou, Green Chem. 19 (2017) 682–691.
[37] M.J. Gilkey, D.G. Vlachos, B. Xu, Appl. Catal. A Gen. 542 (2017) 327–335.
[38] P.A. Webb, C. Orr, Analytical Methods in Fine Particle Technology, Micromeritics Instrument Corp, 1997.
[39] S. Bordiga, E. Groppo, G. Agostini, J.A. van Bokhoven, C. Lamberti, Chem. Rev. 113 (2013) 1736–1850.
[40] S. Nikitenko, A.M. Beale, A.M.J. van der Eerden, S.D.M. Jacques, O. Leynaud, M. G. O'Brien, D. Detollenaere, R. Kaptein, B.M. Weckhuysen, W. Bras, J. Synchroton Rad. 15 (2008) 632–640.
[41] B. Ravel, M. Newville, J. Synchrotron Rad. 12 (2005) 537–541.
[42] S.I. Zabinsky, J.J. Rehr, A. Ankudinov, R.C. Albers, M.J. Eller, Phys. Rev. B 52 (1995) 2995–3009.
[43] S. Calvin, M.M. Miller, R. Goswami, S.-F. Cheng, S.P. Mulvanev, L.J. Whitman, V. G. Harris, J. Appl. Phys. 94 (2003) 778.
[44] F. Niu, S. Xie, Z. Yan, B. Kusema, A.Y. Khodakov, V.V. Ordomsky, Catal. Sci. Technol. 10 (2020) 4396–4404.
[45] A. Tomer, B. Kusema, J.-F. Paul, C. Przybylski, E. Monflier, M. Pera-Titus, A. Ponchel, J. Catal. 368 (2018) 172–189.
[46] K.S. Kim, N. Winograd, J. Catal. 35 (1974) 66–72.
[47] J. Chastain (Ed.), Handbook of X-Ray Photoelectron Spectroscopy, Perkin-Elmer: Eden Pairie, MN, 1992.
[48] A. Salomonsson, R.M. Petoral Jr., K. Uvdal, C. Aulin, P.-O. Käll, L. Ojamäe, M. Strand, M. Sanati, A. Lloyd Spetz, J. Nanopart. Res. 8 (2006) 899–910.
[49] D.J. Morgan, Surf. Interface Anal. 47 (2015) 1072–1079.
[50] C. Eickes, E. Brosha, F. Garzon, G. Purdy, P. Zelenay, T. Morita, D. Thompsett. 3rd International Symposium on Proton Conducting Membrane Fuel Cells, 202nd Meeting of The Electrochemical Society, Salt Lake City, USA, 2002.
[51] D.R. Rolison, P.L. Hagans, K.E. Swider, J.W. Long, Langmuir 15 (1999) 774–779.
[52] A. Burgaev, O.A. Usolsev, A.A. Guda, K.A. Lomachenko, I.A. Pankin, Y.V. Rusalev, H. Emerich, E. Groppo, R. Pellegrini, A.V. Soldatov, J.A. van Bokhoven, C. Lamberti, J. Phys. Chem. C 122 (2018) 12029–12037.
[53] S. Guda, A.A. Guda, M.A. Soldatov, K.A. Lomachenko, A.L. Burgaev, C. Lamberti, W. Gawelda, C. Bessler, G. Smolentsev, A.V. Soldatov, Y. Joly, J. Chem, Theory Comput. 11 (2015) 4512–4521.
[54] J.B. Higgins, R.B. LaPierre, J.L. Schlenker, A.C. Rohrman, J.D. Wood, G.T. Kerr, W. J. Rohrbaugh, Zeolites 8 (1988) 446–452.
[55] J. Perez-Pariente, J. Sanz, V. Fornes, A. Corma, J. Catal. 124 (1990) 217–223.
[56] E. Lipmaa, A. Samoson, M. Magi, J. Am. Chem. Soc. 108 (1986) 1730–1735.
[57] Z.W. Yu, A.M. Zheng, Q.A. Wang, L. Chen, J. Xu, J.P. Amoureux, F. Deng, Angew. Chem., Int. Ed. 49 (2010) 8657–8661.
[58] Z. Zhao, S. Xu, M.Y. Hu, X. Bao, C.H.F. Peden, J. Hu, J. Phys. Chem. C 119 (2015) 1410–1417.
[59] A.J.J. Koekkoek, J.A.R. van Veen, P.B. Gerrtisen, P. Giltay, P.C.M.M. Magusin, E.J. M. Hensen, Microporous Mesoporous Mater. 151 (2012) 34–43.
[60] E. Bourgeat-Lami, P. Massiani, F. Di Renzo, P. Espiau, F. Fajula, Appl. Catal. 72 (1991) 139–152.